AMERICAN SOCIETY FOR MICROBIOLOGY | mBio

Check for updates

| Structural Biology | Research Article

Structural analysis of S-ring composed of FliFG fusion proteins in marine *Vibrio* polar flagellar motor

Norihiro Takekawa,[1] Tatsuro Nishikino,[2] Jun-ichi Kishikawa,[2] Mika Hirose,[2] Miki Kinoshita,[3] Seiji Kojima,[4] Tohru Minamino,[3] Takayuki Uchihashi,[5] Takayuki Kato,[2] Katsumi Imada,[1] Michio Homma[5,6]

AUTHOR AFFILIATIONS See affiliation list on p. 12.

ABSTRACT The marine bacterium *Vibrio alginolyticus* possesses a polar flagellum driven by a sodium ion flow. The main components of the flagellar motor are the stator and rotor. The C-ring and MS-ring, which are composed of FliG and FliF, respectively, are parts of the rotor. Here, we purified an MS-ring composed of FliF–FliG fusion proteins and solved the near-atomic resolution structure of the S-ring—the upper part of the MS-ring—using cryo-electron microscopy. This is the first report of an S-ring structure from *Vibrio*, whereas, previously, only those from *Salmonella* have been reported. The *Vibrio* S-ring structure reveals novel features compared with that of *Salmonella*, such as tilt angle differences of the RBM3 domain and the β-collar region, which contribute to the vertical arrangement of the upper part of the β-collar region despite the diversity in the RBM3 domain angles. Additionally, there is a decrease of the inter-subunit interaction between RBM3 domains, which influences the efficiency of the MS-ring formation in different bacterial species. Furthermore, although the inner-surface electrostatic properties of *Vibrio* and *Salmonella* S-rings are altered, the residues potentially interacting with other flagellar components, such as FliE and FlgB, are well structurally conserved in the *Vibrio* S-ring. These comparisons clarified the conserved and non-conserved structural features of the MS-ring across different species.

IMPORTANCE Understanding the structure and function of the flagellar motor in bacterial species is essential for uncovering the mechanisms underlying bacterial motility and pathogenesis. Our study revealed the structure of the *Vibrio* S-ring, a part of its polar flagellar motor, and highlighted its unique features compared with the well-studied *Salmonella* S-ring. The observed differences in the inter-subunit interactions and in the tilt angles between the *Vibrio* and *Salmonella* S-rings highlighted the species-specific variations and the mechanism for the optimization of MS-ring formation in the flagellar assembly. By concentrating on the region where the S-ring and the rod proteins interact, we uncovered conserved residues essential for the interaction. Our research contributes to the advancement of bacterial flagellar biology.

KEYWORDS flagellar motor, MS-ring, C-ring, basal body

The marine bacterium *Vibrio alginolyticus*—hereinafter referred to as *Vibrio*—has two types of flagella: a polar flagellum for swimming in an aqueous environment and lateral flagella for swarming on the surface (1) (Fig. 1A). The polar and lateral flagella are driven by sodium ion (Na^+) and proton (H^+) flow, respectively. The flagellar motor is a force-generating complex at the flagellum base, consisting of a dozen stator units and a rotor for rotating the flagellar filament, which acts as a helical propeller. The stator is an energy conversion unit composed of two types of membrane proteins: MotA and MotB for the H^+-driven flagellum and PomA and PomB for the Na^+-driven flagellum (2).

Editor Kelly T. Hughes, University of Utah, Salt Lake City, Utah, USA

Address correspondence to Michio Homma, g44416a@cc.nagoya-u.ac.jp, or Katsumi Imada, kimada@chem.sci.osaka-u.ac.jp.

Norihiro Takekawa and Tatsuro Nishikino contributed equally to this article. The order of the two authors was determined by seniority.

The authors declare no conflict of interest.

See the funding table on p. 12.

Received 24 April 2024
Accepted 29 July 2024
Published 6 September 2024

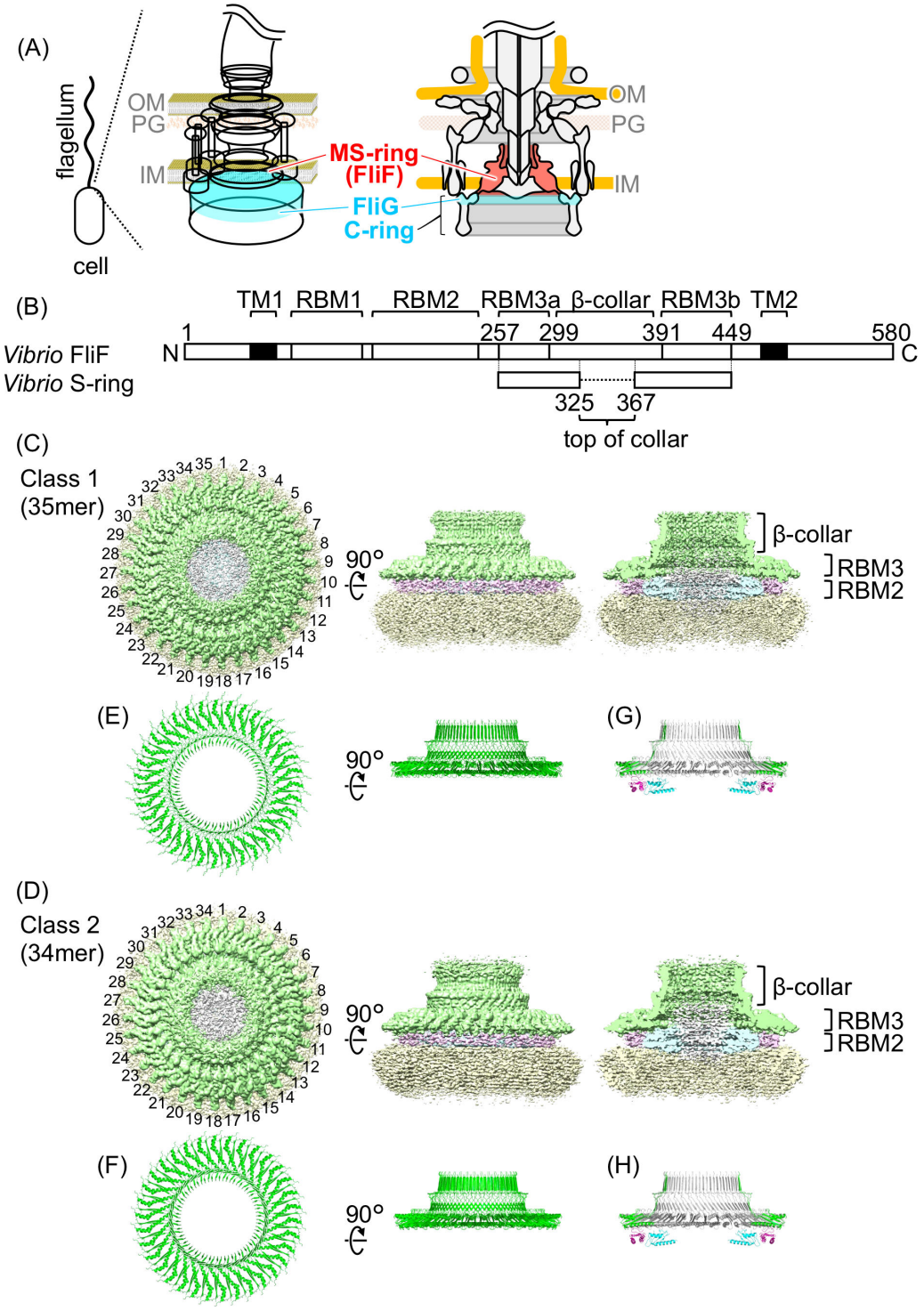

FIG 1 Flagellar motor structure and MS-ring (FliF) in *Vibrio*. (A) Schematic diagram of the flagellar basal body in *Vibrio*. The *Vibrio* cell has a single flagellum at its cell pole, and there is a flagellar motor at the flagellar base. The MS-ring—consisting of FliF—and the upper part of the C-ring—consisting of FliG—are colored with red and cyan, respectively. OM: outer membrane, PG: peptidoglycan layer, IM: inner membrane. (B) Schematic representation of the *Vibrio* FliF primary structure containing the region forming the RBM1, RBM2, RBM3 (divided into RBM3a and RBM3b), β-collar, and transmembrane helices (TM1 and TM2) with residue numbers. The S-ring region built in the model in this study is shown in the lower part. (C and D) Surface representation and vertical section of the cryo-EM map of the purified MS-ring without rotational symmetry correction (C1) of Class 1 (35-mer) and Class 2 (34-mer). Green: S-ring, cyan: inner part of the M-ring, pink: middle part of the M-ring, yellow:

(Continued on next page)

FIG 1 (Continued)

unstructured outermost region of the M-ring, gray: unstructured innermost region. (E and F) The Cα ribbon drawings of the S-ring atomic models built from the maps after rotational symmetry correction (C35 for Class 1 and C34 for Class 2). (G and H) The Cα ribbon drawings of the S-ring atomic models with the previously reported structures of RBM2 (3).

The stator interacts with the rotor—composed of a C-ring and an MS-ring—to generate torque through a gear-like motion (4). The C-ring consists of three soluble proteins, FliG, FliM, and FliN (5, 6), and is composed of ~34, ~34, and ~102 molecules of FliG, FliM, and FliN, respectively (7, 8). MotA or PomA in the stator interact with FliG in the rotor. The C-ring is tightly attached to the MS-ring, which consists of ~34 FliF molecules with two transmembrane helices (3, 9). FliF contains three ring-building motifs (RBM1, RBM2, and RBM3) and β-collar in the periplasmic region between the two transmembrane helices (Fig. 1B). Among these motifs, RBM3–β-collar forms an S-ring on the distal side of the cytoplasm within the MS-ring.

Flagellar construction is postulated to start with the formation of the transmembrane export gate complex and MS-ring, which work as the foundation for flagellar formation (10–12). FliF from *Salmonella enterica* serovar Typhimurium—hereinafter referred to as *Salmonella*—efficiently forms the MS-ring by its overproduction in *Escherichia coli* (13). In this case, the 32–36 RBM3–β-collar subunits form an S-ring, whereas the 21–23 RBM2 subunits form an inner M-ring at the bottom of the S-ring. In addition, the MS-ring, attached to the C-ring, was isolated by the overproduction of *Salmonella* FliF/FliG/FliM/FliN proteins in *E. coli* (14). Using this system, we tried to solve the MS-ring and C-ring structures using cryo-electron microscopy (cryo-EM); however, only RBM3–β-collar and RBM2 of the MS-ring were solved, and it consists of 32 to 34 FliF subunits, with 33 being the most frequently observed in that structure (15), although 33 is thought to be an artificial structure. In the native flagellar structure, the MS-ring contains 34 FliF subunits; 34 RBM3–β-collars form the S-ring, and 23 RBM2s form the inner part of the M-ring in the intact basal body containing the export gate complex and rod in *Salmonella* (9).

Vibrio FliF rarely forms the MS-ring by overproduction in *E. coli* but forms unstructured soluble protein complexes (16). *Vibrio* FliF requires FlhF—an essential factor in the generation of the single polar flagellum in *Vibrio*—to determine the flagellar number at the cell pole along with FlhG or FliG for efficient MS-ring formation in *E. coli*; in other words, *Vibrio* FliF efficiently forms the MS-ring by co-expression with FlhF or FliG (17). During this process, FlhF enhances MS-ring formation by binding to the N-terminal region of FliF (18). A previous structural analysis of the C-ring in *Vibrio* using cryo-electron tomography revealed that the C-ring exhibits a 34-fold rotational symmetry, indicating that the *Vibrio* C-ring comprises 34 molecules of FliG (19). Because FliG and FliF interact in a one-to-one manner, it is assumed that the MS-ring also consists of 34 molecules of FliF in the native flagellar motor in *Vibrio*.

The structure of the *Salmonella* export gate complex—embedded in the M-ring center—was determined to be the $FliP_5FliQ_4FliR_1$ complex (20). The MS-ring structure with the export apparatus and rod complex, the $FliE_6FlgB_5FlgC_6FlgF_5FlgG_{24}$ complex, was determined in the native basal body of the *Salmonella* flagellum (21, 22). The flexible loops at the top of the S-ring interact with FlgB, FlgC, FlgF, and FlgG, the inner surface of the S-ring interacts with FliE and FlgB, and the inner surface of the RBM2 ring interacts with FliQ and FliP to stabilize the export gate complex in the MS-ring (3, 21, 22).

The *fliE*, *fliF*, *fliG*, *fliH*, *fliI*, and *fliJ* genes form operons on the chromosome of *Vibrio*. Based on the report of the functional FliF–FliG fusion protein in *Salmonella* (23), we cloned the *fliF* and *fliG* genes from *Vibrio* into the plasmid and modified them by deletion of a single nucleotide at the 5′-end of the *fliG* start codon to overexpress *Vibrio* FliF–FliG fusion proteins (named FliFG fusion proteins) in *E. coli* (Fig. S1A) (24). The molecular weights of FliF and FliG are ~64 and 39 kDa, respectively, and that of the FliFG fusion protein with an N-terminal His-tag is ~104 kDa. *Vibrio* FliFG fusion proteins efficiently form the MS-ring in *E. coli* (24).

Here, we introduced FliG-G214S or FliG-G215A mutations into *Vibrio* FliFG fusion proteins. The FliG-G214S and FliG-G215A mutations confer strong switch bias and clockwise (CW)-locked rotation of the flagellar motor, respectively (25). The diameter of the C-ring top is 46.2 nm for the FliG-G214S mutant and 49.0 nm for the FliG-G215A mutant, induced by the FliG conformational change by the mutation (19). We performed single-particle cryo-EM of the purified MS-ring formed by FliFG fusion proteins with the FliG-G214S mutation and determined the near-atomic resolution structure of the *Vibrio* S-ring.

RESULTS

Purification of FliFG fusion protein with FliG mutation

We overproduced *Vibrio* His-FliFG fusion proteins with FliG-G214S or FliG-G215A mutation in *E. coli* cells. The membrane fraction containing the MS-ring formed by His-FliFG fusion proteins was treated with the detergent lauryl maltose neopentyl glycol (LMNG), and the MS-ring was precipitated by ultracentrifugation from the detergent-solubilized membrane fraction. We then tried to purify the MS-ring with the His-tag by cobalt-affinity chromatography; however, the MS-ring did not strongly bind to the cobalt column, and most of the MS-ring passed through the column due to unknown causes. The flow-through fraction was ultracentrifuged to precipitate the MS-ring, and the precipitated fraction was subjected to a size-exclusion column (Fig. S1B and C). The MS-ring was recovered near the void fractions as a very large molecular-weight complex. When the void fractions were subjected to sodium dodecyl sulfate-polyacrylamide gel electrophoresis (SDS-PAGE), the FliFG fusion protein (~100 kDa protein band) was detected (Fig. S1D and E). These fractions were observed using electron microscopy (EM).

Cryo-EM structural analysis of the MS-ring formed by FliFG fusion proteins

We observed the purified MS-rings formed by FliFG fusion proteins with FliG-G214S or FliG-G215A mutation by using EM following negative staining (Fig. S2A and B). After the samples were concentrated using an Amicon device, they were applied to an EM grid and rapidly frozen for cryo-EM observation. The MS-ring structure with the FliG-G214S mutation was observed by using cryo-EM (Fig. S2C); however, the MS-ring with the FliG-G215A mutation could not be observed, which was likely due to aggregation during the concentration process of the FliFG-G215A mutant proteins. Therefore, we performed a single-particle cryo-EM of the MS-ring with the FliG-G214S mutation for structure determination. A total of 228,461 particle images extracted from 5,962 cryo-EM micrographs were analyzed. They were separated into two classes in the 2D class averages, with them showing either 35- or 34-fold rotational symmetry on the S-ring (Fig. 1C and D; Fig. S3 and S4D). No other symmetry in the 2D class averages was observed, indicating that the purified MS-ring consisted of 35 or 34 subunits of the FliFG fusion proteins, and there was no other variation. Because the MS-ring in the native flagellar motor is thought to comprise 34 FliF subunits (19), it is inferred that the 34-fold rotational symmetry structure reflects the native S-ring structure, whereas the 35-fold rotational symmetry structure is an artificial structure induced by the overexpression of FliFG fusion proteins alone. After postprocess without symmetry correction, their resolutions of 35 and 34 subunit MS-rings were 3.76 and 4.28 Å, respectively. The MS-ring composed of FliFG fusion proteins purified in this study should include regions other than the S-ring, such as RBM1, RBM2, the two TM helices, the C-terminal region of FliF, and the C-terminally fused FliG. However, structures derived from these regions were not observed with sufficient resolution in our cryo-EM density maps. Therefore, we conducted detailed structural analysis focusing only on the S-ring. Consequently, we built the atomic model of the S-ring part (RBM3–β-collar) at 3.23 and 3.33 Å resolutions from the maps of both classes after C35 and C34 rotational symmetry corrections, respectively (Fig. 1E and F; Fig. S3 and S4). We built the structural model for the S-ring, but due to poor density, we could

not build the model for the M-ring. It is noteworthy that weak densities corresponding to RBM2 were visible, similar in size to the previously reported RBM2 structures at the cross-section from side-views (Fig. 1C, D, G and H), although it was impossible to build the atomic model from our maps.

The S-ring is formed by residues 257–449 of *Vibrio* FliF ($FliF_{257–449}$), which corresponds to the latter half of the periplasmic region (Fig. 1B). The overall monomeric structure of our *Vibrio* S-ring was similar to previously reported monomeric structures of *Salmonella* S-rings (Fig. 2). The $FliF_{257–449}$ monomeric structure consists of two structural regions: a conserved globular RBM3 domain with an αββαβ motif (α1/β1/β6/α2/β7; residues 257–299 and 392–449), and a β-collar (residues 300–388) containing two sets of antiparallel β sheets (β2/β5 and β3/β4) with an invisible region (residues 328–366) at the top of the β-collar (Fig. 2A and B). The monomeric structures in the S-ring part from the 35- and 34-mer structures are almost identical (RMSD = 0.286 Å) (Fig. S5A and B). The monomeric structures of the *Salmonella* S-ring RBM3 were also highly similar to those of *Vibrio*; the RMSDs were less than 1.3 Å (Fig. S5C; Table S3).

S-ring structure comparisons from *Vibrio* and *Salmonella*

We compared the *Vibrio* S-ring FliF 34-mer structure with three previously reported *Salmonella* S-ring FliF 34-mer structures (Fig. 3) where a notable difference is the tilt angle of the RBM3 domain. When measuring the α1 helix angle from the side-view of the ring, the RBM3 outer part is tilted downwards by 8° in the *Vibrio* S-ring, whereas it is tilted upwards by 6° or 8° or is nearly horizontal in the *Salmonella* S-ring (Fig. 3B). When comparing the β2/β5 sheet angles, they all exhibited a similar angle (55°) when viewed from the outside of the ring, whereas the angle is smallest in the *Vibrio* S-ring

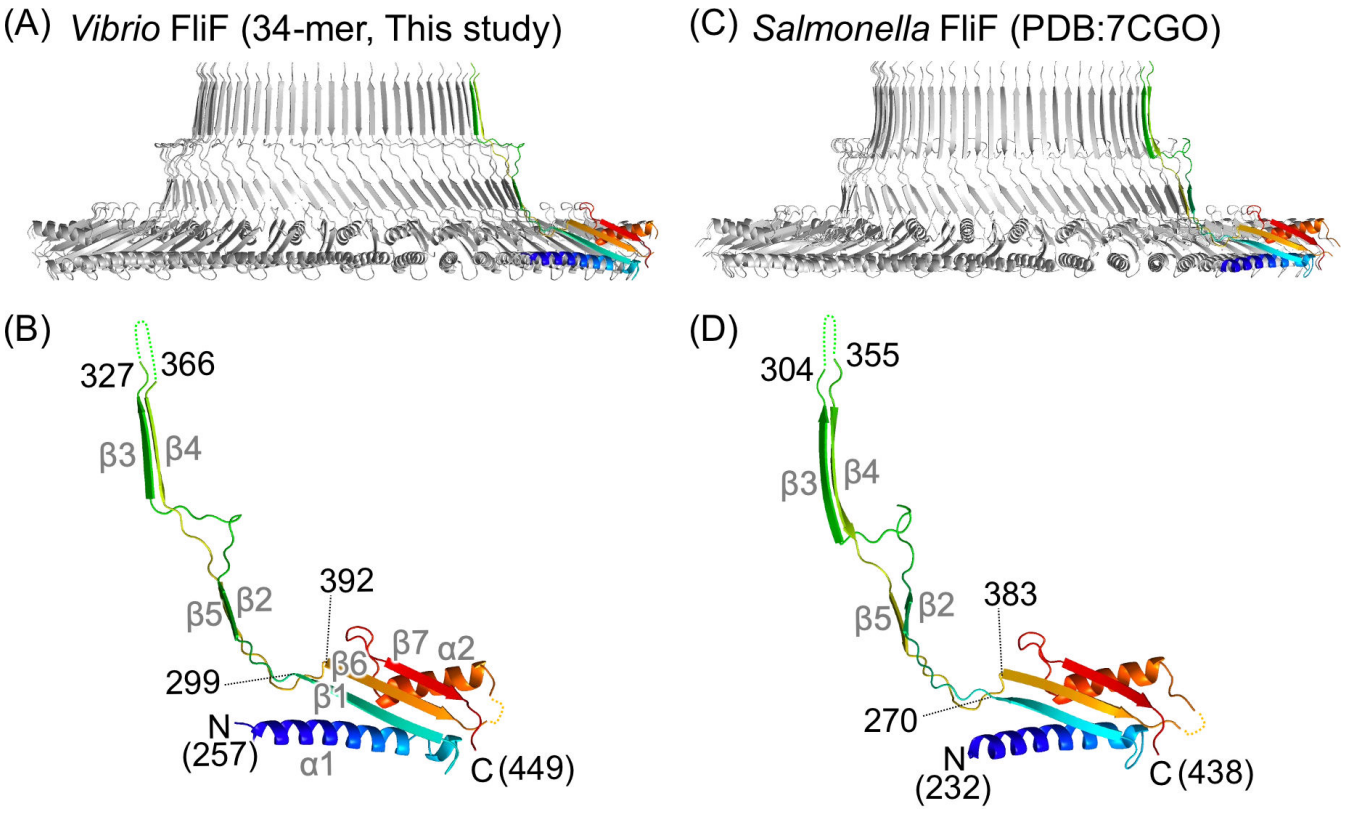

FIG 2 Comparison of the S-ring and FliF structures of *Vibrio* and *Salmonella*. (A) Cross-section view of the *Vibrio* S-ring structure shown as a Cα ribbon drawing. A protomer is colored in rainbow gradient from blue at the N-terminus to red at the C-terminus. (B) Magnified view of the protomer in panel A. (C) Cross-section view of the *Salmonella* S-ring structure. (D) Magnified view of the protomer in panel C. The secondary structure elements are labeled with gray text in panels B and D.

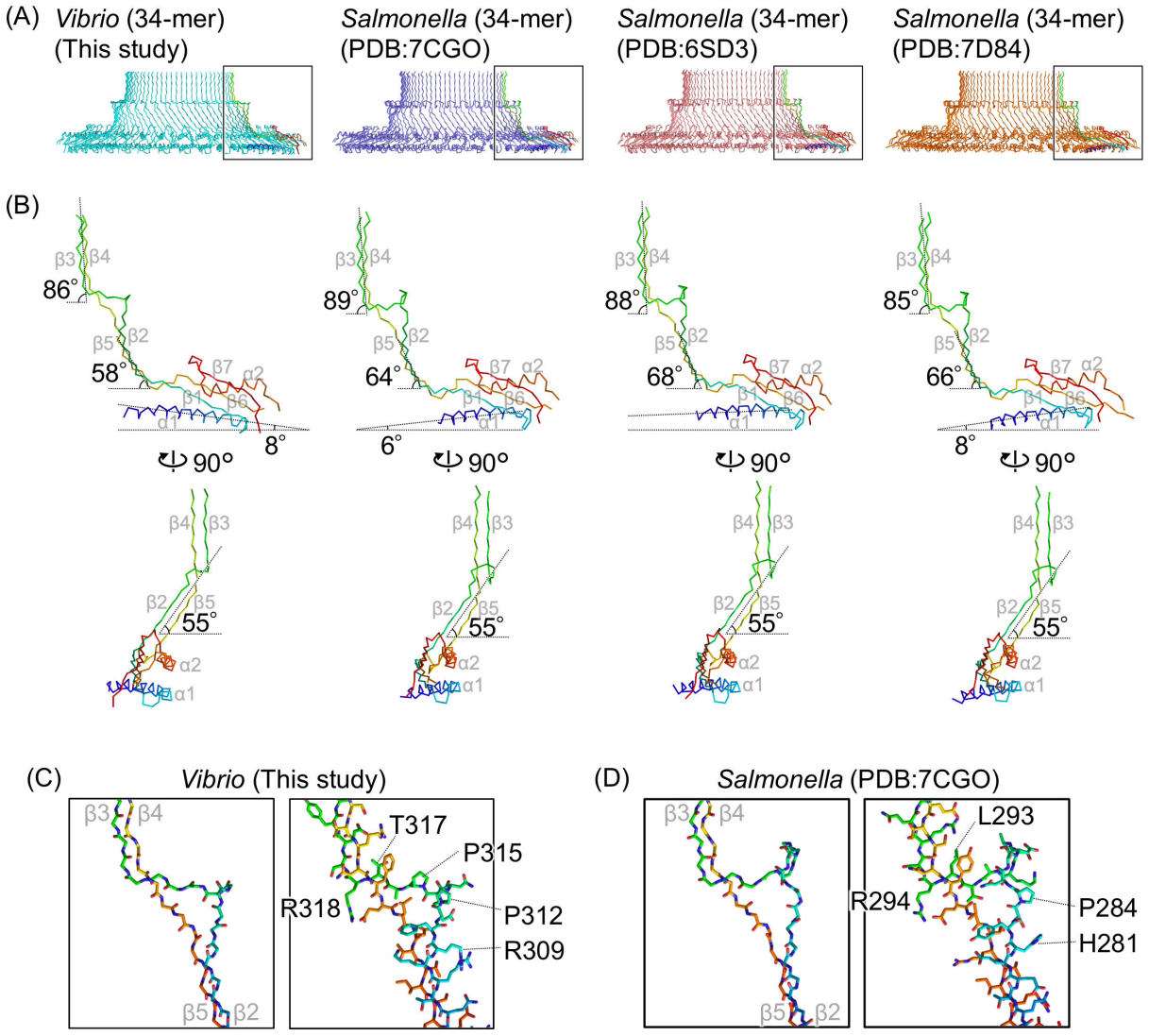

FIG 3 Comparison of the various S-ring and FliF structures. (A) Cross-section view of the Cα ribbon drawing of the S-ring structures from the MS-ring formed by *Vibrio* FliFG fusion protein (34-mer, this study), the intact flagellar hook basal body in *Salmonella* (PDB ID: 7CGO), the MS-ring formed by *Salmonella* FliF (PDB ID: 6SD3), and the MS-ring formed by *Salmonella* FliF (PDB ID: 7D84). All have 34-fold rotational symmetry. A protomer in each ring is colored in rainbow. (B) Comparison of FliF protomer structures in the S-rings. The protomers colored in rainbow in panel A are shown. The inclination angles of the RBM3, the antiparallel β2/β5 strands, or the β3/β4 strands relative to the horizontal are shown. (C and D) Comparison of the protruding triangular β2–β3 loops in *Vibrio* FliF (this study) and *Salmonella* FliF (PDB ID: 7D84) structures. Left: stick models of the main chains. Right: stick models with the side chains. The secondary structure elements are labeled with gray text in panels B–D.

(58°) compared with the *Salmonella* S-ring (64°–68°) when viewed from the side (Fig. 3B). The relative angle variation between the RBM3 and the β2/β5 sheet from the side-view indicates that the linker connecting them is structurally flexible. As for the β3/β4 sheet, all exhibit similar angles of ~85°–89° when viewed from the side (Fig. 3B). Residues 309–318 connecting β2 and β3 form a protruding triangular loop (β2–β3 loop) in the *Vibrio* S-ring, which is shorter than the loop (281–294) in the *Salmonella* S-ring (Fig. 3C and D; Fig. S6A). The relative angles between the β2/β5 sheet and the β3/β4 sheet are observed to be wider in the *Vibrio* S-ring (28°) compared with the *Salmonella* S-rings (19°–25°) (Fig. 3B). This difference arises from variances in the shape of the β2–β3 loop in *Vibrio* and *Salmonella*.

When focusing on the subunit interface of the RBM3 during ring formation, interaction was facilitated by two sites: an electrostatic interaction between E270 and

K276 and a hydrophobic interaction between A399, V429, and L447 in the *Vibrio* S-ring (Fig. 4A and B). These two interaction sites are conserved in the *Salmonella* S-ring, with an electrostatic interaction between E242 and R248 and hydrophobic interactions among V390, L415, and V433. In contrast, the *Salmonella* S-ring has additional hydrophobic interactions among L235, F237, and V241, which are not conserved in *Vibrio* (Fig. 4C and D), indicating that the interaction between the adjacent RBM3 regions in the S-ring is weaker in *Vibrio* than in *Salmonella*.

The internal surface of the S-ring is known to interact with the rod and export gate. Here, we found that the inner surface electrostatic distributions of the S-ring are different between *Vibrio* and *Salmonella* (Fig. 5A and B).

In *Salmonella*, the S-ring internal surface directly interacts with specific regions of FliE and FlgB. Some residues at the inner upper part of the β-collar in FliF (R294/S295/Q297/N365/E367) interact with a flexible loop in the D_C domain in FlgB (residues 58–82), and some residues around the base of the β-collar in FliF (E276/T278/E280/R370/I372/H374) interact with the N-terminal α-helix in FliE (Fig. 5C and D; Fig. S6 and S7) (21, 22, 26, 27). Most of the S-ring residues that interact with FliE or FlgB were conserved in our *Vibrio* S-ring structure, except for Q297 in *Salmonella* (Y321 in *Vibrio*) and E280 and R370 in *Salmonella* (K308 and T379 in *Vibrio*) (Fig. 5D and E; Fig. S6A).

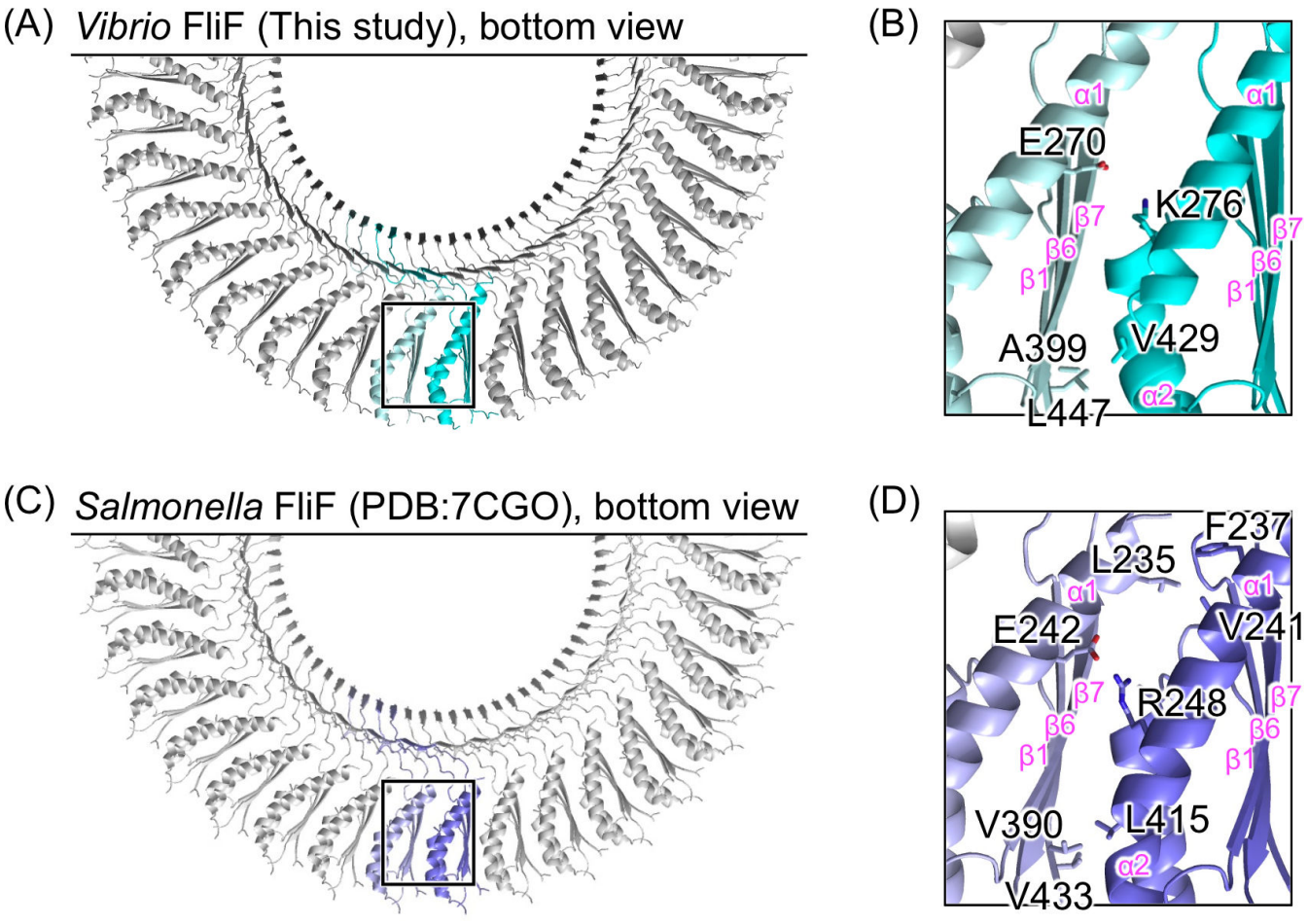

FIG 4 Comparison of the inter-subunit interface in the S-ring of *Vibrio* and *Salmonella*. (A and C) Bottom view of the Cα ribbon drawing of the S-ring structures of *Vibrio* and *Salmonella*. (B and D) Magnified view of the squared region in panels A and C. The side chains contributing to the inter-subunit interaction in the RBM3 are shown in stick models. The secondary structure elements are labeled with pink text in panels B and D.

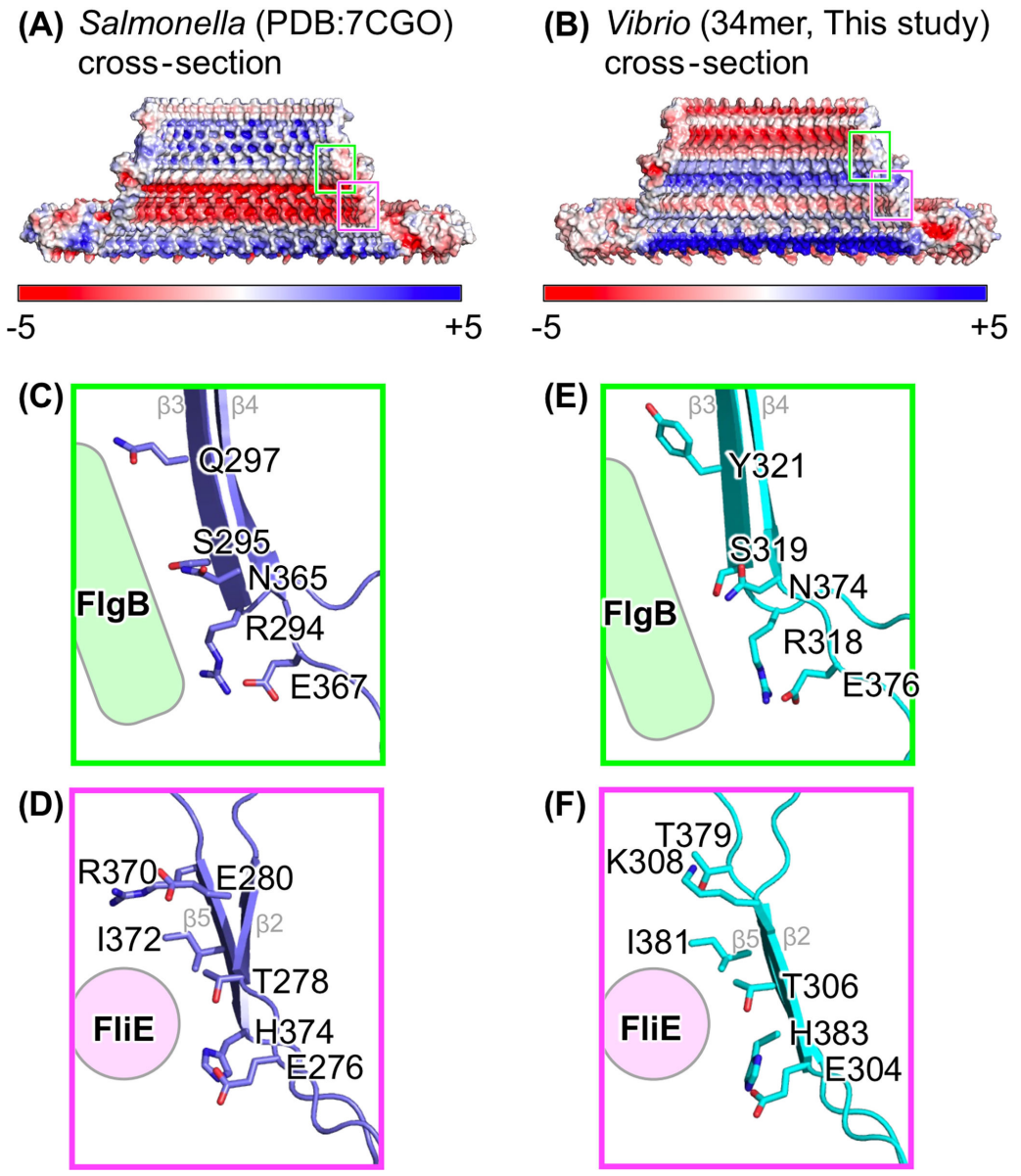

FIG 5 Electrostatic surfaces and regions interacting with rod proteins. (A and B) Cross-section image of the surface model with electrostatic potential of the S-ring structure. (C and D) Magnified views of the cyan and magenta squares in panel A. (E and F) Magnified views of the cyan and magenta squares in panel B. Sidechains contributing to the interaction with FlgB or FliE are shown in stick models. The secondary structure elements are labeled with gray text in panels C–F.

DISCUSSION

In this study, we determined the near-atomic resolution structure of the S-ring (RBM3–β-collar) and the low-resolution structure of the RBM2 region in the MS-ring, composed of FliFG fusion proteins from *Vibrio*. We did not observe other regions, including RBM1, the two TM helices, C-terminal region of FliF, or fused FliG at the C-terminus of the FliFG fusion protein. Structural analysis of the purified MS-ring formed by FliFG fusion proteins using high-speed atomic force microscopy (HS-AFM) showed that it has a flexible structural region derived from the fused FliG around the MS-ring structure (24). Here, we observed MS-rings consisting of FliFG fusion proteins with the FliG-G214S or FliG-G215A mutation by HS-AFM (Movie S1 and S2) and found vague structures at the outer part of the MS-ring, similar to the ring without the FliG mutation (24).

Our S-ring structures are composed of 34 or 35 molecules of the FliFG fusion protein. Their diameters differ: the outer and inner diameters are about 26.0 nm and 9.6 nm, respectively, in the 35-mer ring, and about 25.2 nm and 9.4 nm, respectively, in the 34-mer ring. The difference in the outer and inner circumferences derived from these diameters is approximately 2.4 nm and 0.7 nm, respectively, which are roughly equal to the calculated differences produced by one subunit.

In our two S-ring structures, the 34-mer structure should reflect the native S-ring structure, since the *in situ* MS-ring is a 34-mer of FliF (19). Although *Salmonella* FliF molecules can form MS-rings simply by overexpression alone in *E. coli*, *Vibrio* FliF molecules cannot form these by overexpression alone in *E. coli* but can form by co-expression with FliG or FlhF or by fusion with FliG (24). The differences between *Salmonella* and *Vibrio* may be due to FliF characteristics. In fact, focusing on the inter-subunit interface of the RBM3 regions in the S-ring, *Vibrio* FliF exhibited less hydrophobic interaction than *Salmonella* FliF (Fig. 4). This difference would potentially elucidate why MS-ring formation by FliF alone is less likely to occur in *Vibrio*.

We also found that the tilt angle of the RBM3 in the *Vibrio* S-ring was different from that in *Salmonella* S-rings (Fig. 3B). Because SpoIIIAG—a 30-mer ring component in the feeding tube apparatus in *Bacillus subtilis*—also contains a RBM3-like structure and the corresponding α1 helix is tilted upwards by about 23° (28), the tilt angle of RBM3 might have a little effect on ring formation. The difference in the relative angle between the β2/β5 and the β3/β4 sheets in the *Vibrio* S-ring and the *Salmonella* S-rings (Fig. 3B) is thought to arise from shape differences of the protruding triangular β2–β3 loop, with the length of the loop in *Vibrio* being four amino acids shorter than that in *Salmonella* (Fig. 3C and D). Due to such distinctive differences in the protruding triangular β2–β3 loop, it is presumed that the β3/β4 sheet is arranged vertically in *Vibrio* as well, regardless of tilt angle differences in the RBM3.

The internal surface of the S-ring interacts with the FliE and FlgB rod proteins. Five key residues that interact with FlgB and six key residues that interact with FliE in *Salmonella* are well-conserved in *Vibrio*, except for three residues (K308, Y321, and T379 in *Vibrio* that correspond to E280, Q297, and R370 in *Salmonella*) (Fig. 5C and D). It is possible that these non-conserved residues do not strongly contribute to the interactions with FliE or FlgB, as they are located slightly away from the interacting conserved residues. Alternatively, the non-conserved residues may participate in the interaction specific to *Vibrio*; in fact, the amino acid sequences of the D_C domain in FlgB and the N-terminal α-helix in FliE—potentially interacting with the S-ring—are not fully conserved between *Salmonella* and *Vibrio* (Fig. S6B and C). Despite notable differences in the electrostatic distribution on the S-ring inner wall (Fig. 5A and B), key residues interacting with FlgB and FliE were conserved, indicating that the S-ring does not interact with the rod complex through its entire inner surface, but the specific residues on the inner wall are sufficient for the interaction between the S-ring and the rod.

MATERIALS AND METHODS

Strains, plasmids, and media

The bacterial strains and plasmids used here are listed in Table S1. *E. coli* cells were cultured in LB medium (1% [wt/vol] bactotryptone, 0.5% [wt/vo;] yeast extract, and 0.5% [wt/vol] NaCl). Ampicillin was added at a final concentration of 100 µg/mL. Point mutations (FliG-G214S or FliG-G215A) in plasmid pRO301 were introduced using the QuikChange site-directed mutagenesis method (Agilent).

Purification of the MS-ring composed of the FliFG fusion proteins

An overnight culture of *E. coli* cells containing plasmid (pRO302 or pRO303) was inoculated at 1/50 dilution into 50 mL of LB medium containing ampicillin and grown at 37°C for 4 h. The 20-mL culture was inoculated into 2 L of LB medium containing

ampicillin and grown at 37°C for 3–4 h. When the optical density at 660 nm reached 0.4–0.5, isopropyl-β-D-thiogalactopyranoside was added at 0.5 mM, the culture was cooled on ice for 20 min, and then incubated at 16°C for 20 h. The cells were collected by low-speed centrifugation and the pellet was stored at −20°C, if necessary. The pellet was resuspended in 25 mL of TK buffer (20 mM Tris-HCl [pH 8.0], 200 mM KCl) or TN buffer (20 mM Tris-HCl [pH 8.0], 200 mM NaCl) containing 1mM EDTA.

The suspension was placed in a conical tube and sonicated three times at a power of 6 and 50% duty ratio for 1 min. After low-speed centrifugation, the supernatant was recovered, and the precipitated cells were suspended in 25 mL of TK or TN buffer containing 1 mM EDTA and sonicated again under the same conditions as before (repeated twice in total). A 1/500 vol of 1 M $MgCl_2$ was added to the pooled supernatants and centrifuged at low speed. The resulting supernatant was ultracentrifuged at 150,000 × *g* for 60 min. The precipitates were suspended in 20 mL of TK or TN buffer, and 2 mL of 10% (wt/vol) LMNG was added and incubated at 37°C for 30 min. After low-speed centrifugation, the supernatant was ultracentrifuged at 150,000 × *g* for 60 min. The precipitate was suspended in 1 mL of TK or TN buffer containing 0.01% (wt/vol) LMNG. The suspension was applied to a cobalt column, and the flow-through fraction was ultracentrifuged and suspended in 1 mL of TK or TN buffer containing 0.01% (wt/vol) LMNG. The suspended solutions were subjected to the size-exclusion column (Superose 6 10/300, GE healthcare) equilibrated with TK100L buffer (20 mM Tris-HCl [pH 8.0], 100 mM KCl, 0.0025% [wt/vol] LNMG) or TN100L buffer (20 mM Tris-HCl [pH 8.0], 100 mM NaCl, 0.0025% [wt/vol] LNMG).

Sample preparation and data correction of negative staining images by EM

Elution fractions containing the MS-ring composed of FliFG fusion proteins with the FliG-G214S or FliG-G215A mutations were concentrated five-fold using an Amicon Ultra 100 K device (Merck Millipore). The G214S and G215A mutants were diluted 50- and 100-fold, respectively, in TN100L buffer. A 5-µL solution was applied to a glow-discharged continuous carbon grid. Excess solution was removed using filter paper, and the sample was subsequently stained on a carbon grid with 2% (wt/vol) ammonium molybdate. Images were recorded using a H-7650 transmission electron microscope (Hitachi) operated at 80 kV and equipped with a FastScan-F114 CCD camera (TVIPS) at a nominal magnification of 40,000×.

Cryo-EM observation

A concentrated MS-ring sample composed of the FliFG fusion protein with the FliG-G214S mutation was applied to a Quantifoil holey carbon grid (R1.2/1.3 Cu 300 mesh, Quantifoil Micro Tools GmbH) with glow-discharge treatment on one side of the grid. The grids were placed in liquid ethane cooled with liquid nitrogen for rapid freezing using a Vitrobot Mark IV (Thermo Fisher Scientific) with a blotting time of 7 s at 4°C and 100% humidity. The data were collected on Titan Krios electron microscope (FEI) equipped with a thermal field-emission electron gun operated at 300 kV. Image data sets of 6,372 micrographs collected by a Titan Krios microscope were automatically recorded on a K3 direct electron detector camera (Gatan) at a nominal magnification of 64,000× corresponding to a pixel size of 1.14 Å with a defocus range from −0.7 to −1.7 µm, using the SerialEM software. Micrographs were taken after a total exposure time of 7.329 s, and an electron dose of 0.78 electrons/$Å^2$ per frame. The 64 micrograph frames were recorded at a rate of 0.115 s/frame. The data collection and image analysis are presented in Fig. S3 and Table S2.

Data processing

A total of 6,372 micrographs were motion corrected, and their contrast transfer function (CTF) values were estimated using the CryoSPARC package. A total of 500 micrographs were used for the initial particle picking by using a blob picker. A total of 125,759

particles were automatically extracted from the micrographs, and 2D classification was performed thrice to remove false particles. In total, 15,833 particles selected from the 2D classification were used as input templates for the template picker. A total of 2,059,366 particles were automatically extracted from the micrographs, and 2D classification was performed once to remove false particles. The top or bottom views of the 2D classification averages with 35- or 34-fold rotational symmetries were observed, and all true particles (860,145 particles) were combined for the subsequent 3D classification. *Ab initio* reconstruction was performed to generate two initial 3D models using 512,737 particles selected from the 2D classification. Heterogeneous refinement with C35 symmetry was then performed using two of the three initial models to generate a 3D model with C35 symmetry. Heterogenous refinement was performed with 860,145 particles by using two of three 3D models with C35 symmetry and 2D classification to remove false particles. The remaining 510,049 particles underwent heterogeneous refinement applied individually with C1, C34, and C35 symmetries to generate 3D models. The remaining 320,933 particles from heterogeneous refinement without symmetry (C1) underwent further heterogeneous refinement using the C34 and C35 models. Of these, 261,524 and 55,606 particles remained in classes with C35 and C34 symmetries, respectively. The particles belonging to each class underwent homogenous refinement with C35 and C34 symmetries to generate models for the final heterogeneous refinement to remove false particles. The remaining 183,915 and 43,546 particles with C35 and C34 symmetries, respectively, underwent homogeneous symmetry refinement and Global CTF refinement. Subsequently, the particles with C35 symmetry underwent homogenous refinement, and a map was obtained at 3.23-Å resolution (Class 1; C35). To relax the symmetry, local refinement was performed, and a map was obtained at 3.76-Å resolution (Class 1; C1). Particles with C34 symmetry underwent homogeneous refinement, and a map was obtained at 3.33-Å resolution (Class 2; C34). Moreover, homogenous refinement without symmetry and homogenous refinement were performed, and a map was obtained at 4.28-Å resolution (Class 2; C1). The local resolution of the 3D volumes with C34 and C35 symmetries was estimated using the CryoSPARC package at 0.143 of its Fourier shell correlation threshold.

Model building

The atomic model of the S-ring was constructed from the maps of Class 1 (C35) and Class 2 (C34) using Coot (29) and refined using Phenix (30). The initial models were built from the monomeric RBM3–β-collar structure of *Vibrio* FliF produced by SWISS-MODEL (swissmodel.expasy.org) based on the RBM3–β-collar structure from *Salmonella* (PDB ID: 8T8P). A summary of the model refinement is presented in Table S2. Structural comparisons and analyses were performed using PyMOL (Schrödinger) and Chimera (31).

HS-AFM observation and image analysis

HS-AFM imaging was performed using a laboratory-built HS-AFM operated in the tapping mode, as previously described (24). The MS-rings composed of FliFG fusion proteins were deposited on a bare mica substrate for HS-AFM imaging. After 5 min of incubation, the residual proteins were washed off using observation TN100L buffer. HS-AFM imaging was performed in the sample solution at room temperature.

ACKNOWLEDGMENTS

We thank Dr. Kimika Maki for the technical support with electron microscopic observation to screen the MS-ring samples by negative staining.

This study was partially supported by JSPS KAKENHI Grant Numbers 21H00393, 21H01772, 22K18943 (to T.U.), 23K14158 (to N.T.), 23K18114 (to K.I.) and 20H03220 (to M.H.).

Author contributions: N.T., T.N., and M.H. designed the study; N.T., T.N., M.H., M.K., T.M., T.U., H.K., T.M., and M.H. performed the experiments; J.-I.K., T.K., S.K., N.T., K.I., and M.H. analyzed the data; N.T., K.I., and M.H. wrote the manuscript.

AUTHOR AFFILIATIONS

[1]Department of Macromolecular Science, Graduate School of Science, Osaka University, Toyonaka, Osaka, Japan
[2]Institute for protein research, Osaka University, Suita, Osaka, Japan
[3]Graduate School of Frontier Biosciences, Osaka University, Suita, Osaka, Japan
[4]Department of Biological Science, Graduate School of Science, Nagoya University, Nagoya, Japan
[5]Department of Physics, Graduate School of Science, Nagoya University, Nagoya, Japan
[6]Department of Biomolecular Engineering, Graduate School of Engineering, Nagoya University, Nagoya, Japan

PRESENT ADDRESS

Tatsuro Nishikino, Department of Life Science and Applied Chemistry, Nagoya Institute of Technology, Nagoya, Aichi, Japan
Jun-ichi Kishikawa, Department of Applied Biology, Kyoto Institute of Technology, Matugasaki-Hashiuecho, Kyoto, Japan

AUTHOR ORCIDs

Norihiro Takekawa http://orcid.org/0000-0003-2802-4605
Tatsuro Nishikino http://orcid.org/0000-0001-9950-3086
Seiji Kojima http://orcid.org/0000-0002-5582-8935
Tohru Minamino http://orcid.org/0000-0002-8175-1951
Katsumi Imada http://orcid.org/0000-0003-1342-8885
Michio Homma http://orcid.org/0000-0002-5371-001X

FUNDING

Funder	Grant(s)	Author(s)
MEXT | Japan Society for the Promotion of Science (JSPS)	21H00393,21H01772,22K18943	Takayuki Uchihashi
MEXT | Japan Society for the Promotion of Science (JSPS)	23K14158	Norihiro Takekawa
MEXT | Japan Society for the Promotion of Science (JSPS)	23K18114	Katsumi Imada
MEXT | Japan Society for the Promotion of Science (JSPS)	20H03220	Michio Homma

DATA AVAILABILITY

The cryo-EM maps were deposited in the Electron Microscopy Data Bank under accession codes EMD-39763, EMD-39765, EMD-39761, and EMD-39764. Atomic coordinates were deposited in the Protein Data Bank (www.wwpdb.org) under the accession codes 8Z4G and 8Z4D.

ADDITIONAL FILES

The following material is available online.

Supplemental Material

Supplemental Figures and Tables (mBio01261-24-s0001.pdf). Fig. S1-S7 and Tables S1-S3.
Movie S1 (mBio01261-24-s0002.mp4). HS-AFM movies of the MS-ring composed of FliFG fusion proteins with FliG-G214S mutation. Real-time play speed: 0.15 s/frame.
Movie S2 (mBio01261-24-s0003.mp4). HS-AFM movies of the MS-ring composed of FliFG fusion proteins with FliG-G214S mutation. Real-time play speed: 0.15 s/frame.

REFERENCES

1. Homma M, Nishikino T, Kojima S. 2022. Achievements in bacterial flagellar research with focus on *Vibrio* species. Microbiol Immunol 66:75–95. https://doi.org/10.1111/1348-0421.12954
2. Takekawa N, Imada K, Homma M. 2020. Structure and energy-conversion mechanism of the bacterial Na^+-driven flagellar motor. Trends Microbiol 28:719–731. https://doi.org/10.1016/j.tim.2020.03.010
3. Takekawa N, Kawamoto A, Sakuma M, Kato T, Kojima S, Kinoshita M, Minamino T, Namba K, Homma M, Imada K. 2021. Two distinct conformations in 34 FliF subunits generate three different symmetries within the flagellar MS-ring. mBio 12:e03199-20. https://doi.org/10.1128/mBio.03199-20
4. Terashima H, Kojima S, Homma M. 2021. Site-directed crosslinking identifies the stator-rotor interaction surfaces in a hybrid bacterial flagellar motor. J Bacteriol 203:e00016-21. https://doi.org/10.1128/JB.00016-21
5. Homma M, Aizawa S-I, Dean GE, Macnab RM. 1987. Identification of the M-ring protein of the flagellar motor of *Salmonella typhimurium*. Proc Natl Acad Sci U S A 84:7483–7487. https://doi.org/10.1073/pnas.84.21.7483
6. Ueno T, Oosawa K, Aizawa S. 1994. Domain structures of the MS ring component protein (FliF) of the flagellar basal body of *Salmonella typhimurium*. J Mol Biol 236:546–555. https://doi.org/10.1006/jmbi.1994.1164
7. Stock D, Namba K, Lee LK. 2012. Nanorotors and self-assembling macromolecular machines: the torque ring of the bacterial flagellar motor. Curr Opin Biotechnol 23:545–554. https://doi.org/10.1016/j.copbio.2012.01.008
8. McDowell MA, Marcoux J, McVicker G, Johnson S, Fong YH, Stevens R, Bowman LAH, Degiacomi MT, Yan J, Wise A, Friede ME, Benesch JLP, Deane JE, Tang CM, Robinson CV, Lea SM. 2016. Characterisation of *Shigella* Spa33 and *Thermotoga* FliM/N reveals a new model for C-ring assembly in T3SS. Mol Microbiol 99:749–766. https://doi.org/10.1111/mmi.13267
9. Kawamoto A, Miyata T, Makino F, Kinoshita M, Minamino T, Imada K, Kato T, Namba K. 2021. Native flagellar MS ring is formed by 34 subunits with 23-fold and 11-fold subsymmetries. Nat Commun 12:4223. https://doi.org/10.1038/s41467-021-24507-9
10. Kubori T, Yamaguchi S, Aizawa S. 1997. Assembly of the switch complex onto the MS ring complex of *Salmonella typhimurium* does not require any other flagellar proteins. J Bacteriol 179:813–817. https://doi.org/10.1128/jb.179.3.813-817.1997
11. Fukumura T, Makino F, Dietsche T, Kinoshita M, Kato T, Wagner S, Namba K, Imada K, Minamino T. 2017. Assembly and stoichiometry of the core structure of the bacterial flagellar type III export gate complex. PLoS Biol 15:e2002281. https://doi.org/10.1371/journal.pbio.2002281
12. Morimoto YV, Ito M, Hiraoka KD, Che YS, Bai F, Kami-Ike N, Namba K, Minamino T. 2014. Assembly and stoichiometry of FliF and FlhA in *Salmonella flagellar* basal body. Mol Microbiol 91:1214–1226. https://doi.org/10.1111/mmi.12529
13. Oosawa K, Ueno T, Aizawa S. 1994. Overproduction of the bacterial flagellar switch proteins and their interactions with the MS ring complex *in vitro*. J Bacteriol 176:3683–3691. https://doi.org/10.1128/jb.176.12.3683-3691.1994
14. Lux R, Kar N, Khan S. 2000. Overproduced *Salmonella typhimurium* flagellar motor switch complexes. J Mol Biol 298:577–583. https://doi.org/10.1006/jmbi.2000.3703
15. Singh PK, Cecchini G, Nakagawa T, Iverson TM. 2023. CryoEM structure of a post-assembly MS-ring reveals plasticity in stoichiometry and conformation. PLoS One 18:e0285343. https://doi.org/10.1371/journal.pone.0285343
16. Ogawa R, Abe-Yoshizumi R, Kishi T, Homma M, Kojima S. 2015. Interaction of the C-terminal tail of FliF with FliG from the Na^+-driven flagellar motor of *Vibrio alginolyticus*. J Bacteriol 197:63–72. https://doi.org/10.1128/JB.02271-14
17. Terashima H, Hirano K, Inoue Y, Tokano T, Kawamoto A, Kato T, Yamaguchi E, Namba K, Uchihashi T, Kojima S, Homma M. 2020. Assembly mechanism of a supramolecular MS-ring complex to initiate bacterial flagellar biogenesis in *Vibrio* species. J Bacteriol 202:e00236-20. https://doi.org/10.1128/JB.00236-20
18. Fukushima Y, Homma M, Kojima S. 2023. Interaction of FlhF, SRP-like GTPase with FliF, MS ring component assembling the initial structure of flagella in marine *Vibrio*. J Biochem 174:125–130. https://doi.org/10.1093/jb/mvad029
19. Carroll BL, Nishikino T, Guo W, Zhu S, Kojima S, Homma M, Liu J. 2020. The flagellar motor of *Vibrio alginolyticus* undergoes major structural remodeling during rotational switching. Elife 9:e61446. https://doi.org/10.7554/eLife.61446
20. Kuhlen L, Abrusci P, Johnson S, Gault J, Deme J, Caesar J, Dietsche T, Mebrhatu MT, Ganief T, Macek B, Wagner S, Robinson CV, Lea SM. 2018. Structure of the core of the type III secretion system export apparatus. Nat Struct Mol Biol 25:583–590. https://doi.org/10.1038/s41594-018-0086-9
21. Tan J, Zhang X, Wang X, Xu C, Chang S, Wu H, Wang T, Liang H, Gao H, Zhou Y, Zhu Y. 2021. Structural basis of assembly and torque transmission of the bacterial flagellar motor. Cell 184:2665–2679. https://doi.org/10.1016/j.cell.2021.03.057
22. Johnson S, Furlong EJ, Deme JC, Nord AL, Caesar JJE, Chevance FFV, Berry RM, Hughes KT, Lea SM. 2021. Molecular structure of the intact bacterial flagellar basal body. Nat Microbiol 6:712–721. https://doi.org/10.1038/s41564-021-00895-y
23. Francis NR, Irikura VM, Yamaguchi S, DeRosier DJ, Macnab RM. 1992. Localization of the *Salmonella typhimurium* flagellar switch protein FliG to the cytoplasmic M-ring face of the basal body. Proc Natl Acad Sci U S A 89:6304–6308. https://doi.org/10.1073/pnas.89.14.6304
24. Takahashi K, Nishikino T, Kajino H, Kojima S, Uchihashi T, Homma M. 2023. Ring formation by *Vibrio* fusion protein composed of FliF and FliG, MS-ring and C-ring component of bacterial flagellar motor in membrane. Biophys Physicobiol 20:e200028. https://doi.org/10.2142/biophysico.bppb-v20.0028
25. Nishikino T, Zhu S, Takekawa N, Kojima S, Onoue Y, Homma M. 2016. Serine suppresses the motor function of a periplasmic PomB mutation in the *Vibrio* flagella stator. Genes Cells 21:505–516. https://doi.org/10.1111/gtc.12357
26. Minamino T, Yamaguchi S, Macnab RM. 2000. Interaction between FliE and FlgB, a proximal rod component of the flagellar basal body of *Salmonella*. J Bacteriol 182:3029–3036. https://doi.org/10.1128/JB.182.11.3029-3036.2000
27. Hendriksen JJ, Lee HJ, Bradshaw AJ, Namba K, Chevance FFV, Minamino T, Hughes KT. 2021. Genetic analysis of the *Salmonella* FliE protein that forms the base of the flagellar axial structure. mBio 12:e0239221. https://doi.org/10.1128/mBio.02392-21
28. Zeytuni N, Hong C, Flanagan KA, Worrall LJ, Theiltges KA, Vuckovic M, Huang RK, Massoni SC, Camp AH, Yu Z, Strynadka NC. 2017. Near-atomic resolution cryoelectron microscopy structure of the 30-fold homooligomeric SpoIIIAG channel essential to spore formation in *Bacillus subtilis*.

Proc Natl Acad Sci U S A 114:E7073–E7081. https://doi.org/10.1073/pnas.1704310114
29. Emsley P, Lohkamp B, Scott WG, Cowtan K. 2010. Features and development of Coot. Acta Crystallogr D Biol Crystallogr 66:486–501. https://doi.org/10.1107/S0907444910007493
30. Liebschner D, Afonine PV, Baker ML, Bunkóczi G, Chen VB, Croll TI, Hintze B, Hung LW, Jain S, McCoy AJ, Moriarty NW, Oeffner RD, Poon BK, Prisant MG, Read RJ, Richardson JS, Richardson DC, Sammito MD, Sobolev OV, Stockwell DH, Terwilliger TC, Urzhumtsev AG, Videau LL, Williams CJ, Adams PD. 2019. Macromolecular structure determination using X-rays, neutrons and electrons: recent developments in Phenix. Acta Cryst D Struct Biol 75:861–877. https://doi.org/10.1107/S2059798319011471
31. Pettersen EF, Goddard TD, Huang CC, Couch GS, Greenblatt DM, Meng EC, Ferrin TE. 2004. UCSF Chimera--a visualization system for exploratory research and analysis. J Comput Chem 25:1605–1612. https://doi.org/10.1002/jcc.20084